ACCEPTED MANUSCRIPT

Continuous precision separation of gold using a metal-organic framework/polymer composite

To cite this article before publication: Emily Mitchell et al 2023 Nanotechnology in press https://doi.org/10.1088/1361-6528/ad1447

Manuscript version: Accepted Manuscript

Accepted Manuscript is "the version of the article accepted for publication including all changes made as a result of the peer review process, and which may also include the addition to the article by IOP Publishing of a header, an article ID, a cover sheet and/or an 'Accepted Manuscript' watermark, but excluding any other editing, typesetting or other changes made by IOP Publishing and/or its licensors"

This Accepted Manuscript is © 2023 IOP Publishing Ltd.

During the embargo period (the 12 month period from the publication of the Version of Record of this article), the Accepted Manuscript is fully protected by copyright and cannot be reused or reposted elsewhere.

As the Version of Record of this article is going to be / has been published on a subscription basis, this Accepted Manuscript will be available for reuse under a CC BY-NC-ND 3.0 licence after the 12 month embargo period.

After the embargo period, everyone is permitted to use copy and redistribute this article for non-commercial purposes only, provided that they adhere to all the terms of the licence https://creativecommons.org/licences/by-nc-nd/3.0

Although reasonable endeavours have been taken to obtain all necessary permissions from third parties to include their copyrighted content within this article, their full citation and copyright line may not be present in this Accepted Manuscript version. Before using any content from this article, please refer to the Version of Record on IOPscience once published for full citation and copyright details, as permissions may be required. All third party content is fully copyright protected, unless specifically stated otherwise in the figure caption in the Version of Record.

View the article online for updates and enhancements.

Continuous Precision Separation of Gold using a Metal-organic Framework/Polymer Composite

Emily Mitchell^{1,2}, Dana Hernandez^{1,2}, Ashlin Deatherage^{1,2}, Martin Coull¹, M. Virginia Altoé², Liana Klivansky², Matthew Witman¹ and Daniel T. Sun^{1,2,*}

- ¹ Sunchem Inc., 395 South Van Ness Ave, San Francisco, CA 94103, United States of America
- ² Molecular Foundry, Lawrence Berkeley National Laboratory, 1 Cyclotron Rd, Berkeley, CA 94720, United States of America
- *E-mail: daniel.sun@sunchem.io or dtsun@lbl.gov

Received xxxxxxx Accepted for publication xxxxxxx Published xxxxxxx

Abstract

Critical metals of environmental and economic relevance can be found within complex mixtures, such as mine tailings, electronic waste and wastewater, at trace amounts. Specifically, gold is a critical metal that carries desired redox active properties in various applications, including modern electronics, medicine and chemical catalysis. Here we report the structuring of sub-micron Fe-BTC/PpPDA crystallites into larger 250 µm or 500 µm granules for continuous packed bed experiments for the precision separation of gold. The Structured Fe-BTC/PpPDA is highly crystalline and porous with a BET surface area of 750 m² g⁻¹. Further, the hybrid nanocomposite material maintains its selectivity for gold ions over common inorganic interferents. The structuring approach reported prevents excessive pressure drop and ensures stability over time and operation in a packed bed column. Further, we demonstrate that the Structured Fe-BTC/PpPDA can concentrate at least 42 wt. % of gold under a dynamic continuous flow operation. These findings highlight the potential of Structured Fe-BTC/PpPDA for practical applications in industry, particularly in the selective capture of gold from complex mixtures.

Keywords: Precision Separations, Gold, Metal-organic Frameworks/Polymer Composite, Continuous Packed Bed Columns, Mining, Critical Metals

1. Introduction

The precision separation of critical metals from complex mixtures is of both environmental and economic significance^{1,2,3}. Recently, there has been a historic investment and effort in developing

novel sustainable technologies to separate and purify these highly valued critical metals⁴. Gold, for example, is an extremely valuable commodity (value in May 2023: \$ 64,811.00 per kg) and has significant economic relevance⁵. This stems from its rarity and desired redox-active properties that are employed in modern-day electronics, chemical catalysis, and other material applications^{3,6,7,8}. Sources of gold include traditional mining operations, electronic waste, industrial effluent, and surface water near dated mining closures. A significant challenge for its extraction and purification is that gold tends to exist at trace amounts in complex mixtures containing high concentrations of both inorganic and organic interferents^{9,10,11,12}. Therefore, advancing the precision separation of gold, and other critical metals, with adsorption technologies is crucial for our future economy's resiliency and for improving the environmental sustainability of the metals' life cycles.

High porosity and functionality are some of the most sought properties in the discovery of new materials for precision adsorption separation processes. It offers quick diffusion and high adsorption capacities for targeted chemical species significantly reducing energy and operating costs³. Consequently, Metal-organic Frameworks (MOFs) have quickly garnered attention for separations^{13,14,15}. This class of materials has unprecedented internal surface areas, as the highest reported to date is 7800 m² g⁻¹; and therefore have an extraordinary ability to absorb large quantities of guest species^{16,17,18,19,20}. A variety of MOFs are well known for high performance in gas/liquid separations and adsorption^{13,21,22}, but recently, *in-situ* polymerization in MOF pores has generated novel inner pore structural modifications, which can significantly enhance the MOF's performance for critical metal extraction^{23,24,25,26,27,28,29,30,31}.

Previous work demonstrated a novel MOF/Polymer composite material, Fe-BTC/PpPDA [BTC = 1,3,5-benzenetricarboxylate and PpPDA = poly(para-phenylenediamine)], which can selectively and rapidly extract trace amounts of gold from many complex water mixtures including wastewater, fresh water, ocean water, and solutions used to leach gold into water from electronic waste and incinerated sewage sludge²⁹. The new hybrid material has an exceptional adsorption capacity of 934 mg gold per gram of material and rapid adsorption kinetics²⁹. Further, due to the high cyclability, it was demonstrated that the composite can effectively concentrate gold and yield purities up to 23.9 K²⁹. The material demonstrated superior performance under batch adsorption conditions relative to continuous flow, signifying that material refinement is necessary for large-scale applicability.

Industrial implementation necessitates material engineering and assessment of the MOF/polymer under continuous flow operations to implement effective filter devices when large volume streams must be processed. Here we report the structuring of sub-micron Fe-BTC/PpPDA particles (<500 nm) into larger spherical-shaped granules (>250 μm) via granulation with a fluorinated binder, which can improve stability³² of the as-synthesized powder. Next, we perform detailed characterization studies to understand how well the structured materials preserve the desired properties of the Fe-BTC/PpPDA composite. Two structuring methods are investigated: (1) G/Fe-BTC/PpPDA particles are agglomerated only through physical granulation with a fluorinated binder vs. (2) Structured Fe-BTC/PpPDA particles are agglomerated through granulation with a fluorinated binder, followed by freeze drying and heating processes. The performance of both materials for continuous gold extraction in packed bed columns is investigated. We demonstrate that Structured Fe-BTC/PpPDA can indeed selectively extract trace gold during continuous flow operations from water concentrating up to 42 wt.% gold per gram of Structured Fe-BTC/PpPDA material, while preventing excessive pressure drop and maintaining stability over time and operation.

This study introduces a novel packed-bed continuous flow precision separation method for gold using a highly selective MOF/polymer composite, Fe-BTC/PpPDA. The Structured Fe-BTC/PpPDA material showcases exceptional potential for water treatment applications, offering precise gold separation and high gold concentration under dynamic continuous flow conditions. The structuring of submicron Fe-BTC/PpPDA into larger, robust granules (>250 µm) using our approach paves the way for scalable and sustainable applications in water treatment and beyond for this relatively new class of materials. This new method marks a significant stride towards resource-efficient and environmentally conscious gold recovery techniques, offering new horizons for future research and practical implementation in diverse industrial settings.

2. Materials and Methods

Chemicals

1,3,5-benzenetricarboxylic acid (98%) and iron (III) chloride hexahydrate (97%) were bought from Thermo Scientific. P-phenylenediamine (98%) was bought from Sigma-Aldrich and gold (III) chloride (99.99% Au) was bought from BTC Beantown Chemical. Ethanol was bought from Macron Fine Chemicals at Avantor. HPLC grade Methanol was bought from Supelco at the EMD

Millipore Corporation. Hydrochloric acid (36.5% - 38%) was bought from VWR Chemicals. All chemicals were used without further purification. The fluorinated binder was provided by Arkema.

Synthesis of Fe-BTC

In a 2000 mL Pyrex bottle 145.8 g of iron (III) chloride hexahydrate, 50.4 g of trimesic acid, and 1800 mL of distilled water are mixed together. The Pyrex bottle was capped with a PTFE lined DURAN GL45 cap. The reaction mixture was heated at 110 °C for 3 days. The reaction is cooled to room temperature, and then the Fe-BTC mixture is filtered and washed with distilled water and methanol. The Fe-BTC mixture is loaded into cellulose extraction thimbles and undergoes a soxhlet purification with methanol for 24 hours. After purification, the Fe-BTC is dried under vacuum using an Edwards RV5 Rotary Vane Vacuum Pump overnight and is ready for Fe-BTC/PpPDA synthesis. Fe-BTC is activated under vacuum at 150 °C for 15 hours using a Schlenk line and an oil pump before nitrogen adsorption and standard characterization.

Synthesis of Fe-BTC/PpPDA

7.5 g of room-temperature activated Fe-BTC is placed in a three neck 2000 mL round bottom flask and is flushed with nitrogen gas. In a separate three neck 2000 mL round bottom flask, 9.0 g of p-phenylenediamine and 1500 mL of ethanol were loaded and capped with a septum. The ethanol solution is then transferred air free via a steel cannula and nitrogen gas. The reaction mixture stirs at 420 rpm for one hour, and then is exposed to air and heated to 50 °C for 24 hours. The mixture is then filtered and washed with distilled water. The resulting black powder is filtered via vacuum filtration and undergoes soxhlet purification with ethanol for 24 hours. After purification, the sample is dried under vacuum using an Edwards RV5 Rotary Vane Vacuum Pump and is complete. Fe-BTC/PpPDA is activated under vacuum at 125 °C overnight for 15 hours before nitrogen adsorption and standard characterization.

Granulated and Structured Fe-BTC/PpPDA

Fe-BTC/PpPDA granules are made using a custom built disc granulator (Figure S1) of 6 inches in diameter. Two to three grams of the Fe-BTC/PpPDA powder and 10 wt.% of a fluorinated binder are mixed together and loaded into the disc granulator. The powder mixture rotates at an incline angle of around 120° - 180° relevant to the table surface at low speeds, ranging from 10-50 rpm. After a few seconds, the incline angle is adjusted to 90° - 120° at 50 rpm. Spheres will begin to

form, and adding distilled water to the powder mixture aids in spherical particle formation. The granulated Fe-BTC/PpPDA and binder are loaded into various sieves ranging from >53 μm to 850 μm. A minimum of 1 g of 250 μm and 1 g of 500 μm spherical particles are collected for further characterization. The 250 μm and 500 μm granules are freeze-dried for 2 hours using liquid nitrogen and heated at 150°C for 2 hours before column experiments. The resulting material is called Structured Fe-BTC/PpPDA (Figure 1). The granules are then comprehensively analyzed via the characterization techniques below. Note that particles that are formed via the granulation and addition of 10 wt.% fluorinated binder process described above but without freeze-drying nor heating processes are referred to as G/Fe-BTC/PpPDA.

Characterization

Powder x-ray diffraction (PXRD), nitrogen adsorption isotherms (BET), thermogravimetric analyzer (TGA), Fourier transform infrared spectroscopy (FTIR), attenuated total reflection infrared spectroscopy (ATR-IR), inductively coupled plasma optical emission spectroscopy (ICP-OES), x-ray photoelectron spectroscopy (XPS), high resolution analytical field emission scanning electron microscopy (SEM), tabletop SEM, and x-ray energy dispersive spectroscopy (EDS) were instruments used during characterization process in our work, as explained in the supplementary information.

Batch and Kinetic Au Extraction Experiments

Two separate batch experiments were conducted, one with tap water provided at the Molecular Foundry (Latitude: 37.87505, Longitude: -122.24264) and another with Strawberry Creek (Latitude: 37.87419, Longitude: -122.26166) water in Berkeley, California, to test gold extraction capabilities in different matrices containing competing ions and organics, including calcium, potassium, magnesium, strontium, sulfur, and sodium. The pH of the gold-spiked tap and creek water was ~7. Duplicate experiments were conducted on Fe-BTC/PpPDA and Structured Fe-BTC/PpPDA to observe gold uptake in 200 mL beakers. 100 mL of tap or Strawberry Creek water was spiked with 10 ppm gold (III) chloride. 10 mg sample material of either Fe-BTC/PpPDA or Structured Fe-BTC/PpPDA was added to the water sample. They were mixed overnight at 420 rpm with magnetic stir bars and covered with parafilm at room temperature. The following day aliquots were taken and filtered for ICP-OES analysis using three to five different wavelengths for each element to ensure the ICP-OES captured the gold signals. For the kinetics study, 5 mL

aliquots were taken at different time points of 0, 0.5, 1, 2.5, 5, 10, 20, and 30 minutes after the addition of the materials and filtered prior to ICP-OES to remove any solids for elemental analysis of the water²⁹. We also took an aliquot after 15 hours of overnight mixing with our materials. Water samples were filtered using a 5 mL BD Syringe with a Slip Tip attached with an Acrodisc LC 25 mm Syringe Filter. 0.25 mL of 37% concentrated HCl was put into 5 mL of every batch sample prior to ICP-OES.

Packed Bed Column Au Extraction Experiments

Continuous flow experiments were performed in different sized packed bed columns to analyze their breakthrough curve. We started with seven *small* column experiments that have an internal diameter of 0.15 inches and a height of 2.5 inches. Column 1 is filled with 300 mg of 500 µm G/Fe-BTC/PpPDA. Columns 2 and 3 are filled with 300 mg of 500 µm Structured Fe-BTC/PpPDA material. Columns 4, 5, and 6 are filled with 300 mg of 250 µm Structured Fe-BTC/PpPDA material. All columns are filled with 200 mg of glass beads (100 mg on both ends of the column), glass wool with a diameter of 0.15 inches at the tip of the columns, and 0.15 inch in diameter 250 µm stainless steel mesh grids at the inlet and outlet of the columns. A pressure gauge was placed at the inlet of the column to measure pressure across the column bed. Water is first pumped through the columns to ensure a consistent desired flow rate. Afterwards, water spiked with approximately 10 ppm gold (III) chloride is pumped through the column at a flow rate of 10 mL min⁻¹. Effluent water samples are taken at different times and analyzed with ICP-OES to determine the gold concentration and obtain the breakthrough curves.

The *large* column experiment has an internal diameter of 0.375 inches and a height of 9.85 inches. The column is filled with 6.0 g of Structured Fe-BTC/PpPDA (250 µm, 2.0 g of glass beads (1.0 g on both ends of the column), and glass wool with a diameter of 0.375 inches at the tip of the column. The packed bed column is pumped with water for 5 minutes to ensure a consistent 5 mL min⁻¹ flow rate. Afterwards, tap water spiked with approximately 10 ppm Au is pumped through the column at a flow rate of 5 mL min⁻¹. Water is sampled after it has passed through the column at different time points and analyzed with ICP-OES to determine the gold concentration and produce breakthrough curves.

3. Results and Discussion

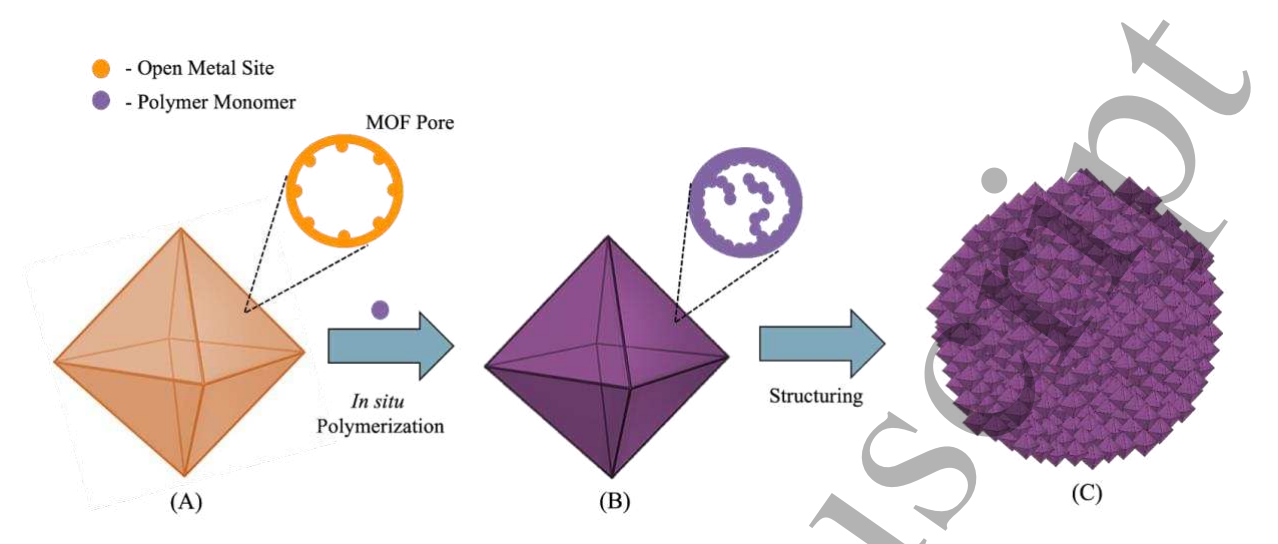


Figure 1. Blueprint for Structured Fe-BTC/PpPDA. The MOF, Fe-BTC (**A**), offers open Fe³⁺ metal sites (as shown in the orange circle) throughout its structure, which can facilitate *in situ* oxidation polymerizations. P-phenylenediamine is introduced into Fe-BTC and the amine (-NH₂) functional groups are oxidized via the Fe³⁺ open metal sites into imines (=NH) resulting in the formation of poly-p-phenylenediamine inside the MOF's porous network (**B**). To make materials accessible for continuous flow packed bed columns, Structured Fe-BTC/PpPDA is formed (**C**), by aggregating Fe-BTC/PpPDA's nm particles together to form larger 250 μm and 500 μm granules.

Although batch adsorption experiments can provide information to initially assess materials^{33,34}, continuous packed bed adsorption experiments must be conducted to obtain other crucial information such as breakthrough time and the maximum capacity of the column device under the continuous dynamic conditions typically employed in industry^{28,35}. The Fe-BTC/PpPDA is first prepared by synthesizing the microcrystalline Fe-BTC structure, which acts as the rigid porous template, and is composed of Fe trimer clusters that are linked together by benzenetricarboxylate ligands³⁰ (Figure 1A).

By taking advantage of the unsaturated open metal sites along the Fe-BTC's pore surface, p-phenylenediamine is introduced into the MOFs porous network and undergoes an *in-situ* polymerization process hybridizing the two components, creating Fe-BTC/PpPDA²⁹ (Figure 1B). Fe-BTC/PpPDA acts as a porous template and introduces extrinsic porosity to intrinsically non-porous polymers giving rise to high surface area accessible adsorption sites pinned along the MOF's interior nanopore surface. The FeBTC/PpPDA material retains its porous nature, mechanical properties of the MOF, and the chemical functionality of the polymer all in one material system.

Characterization of Fe-BTC, Fe-BTC/PpPDA and Structured Fe-BTC/PpPDA

Prior to synthesizing Fe-BTC/PpPDA, PXRD is performed on the porous template Fe-BTC first to confirm the correct phase and high crystallinity (Figure 2A) of the framework. Fe-BTC, also known as MIL-100(Fe) (MIL: Materials of Institut Lavoisier), is a previously reported iron(III) benzene tricarboxylate crystalline material⁴⁵ reported by Horcajada and Férey. The diffraction pattern illustrates the simulated Fe-BTC (black) produced from MercuryTM crystallographic software³⁶. Although the peaks tend to be broader and have slightly lower peak ratios, the PXRD diffraction pattern of the as-synthesized Fe-BTC confirms the correct phase and high crystallinity. The increased broadness of the peaks is likely due to the small nm size (<500nm) of the Fe-BTC particles.

The crystal structure is built from trimers of iron octahedra sharing μ 3-O, to which the oxygen atom connects the three iron(III) ions together representing the secondary building unit (SBU) of this particular MOF structure. The trimers are linked together by the benzene-1,3,5-tricarboxylate moieties that lead to super tetrahedra, and to zeolitic architecture. Specifically, zeolite MTN topology is characterized by three-dimensional frameworks of interconnected channels and cages within a structure. As MIL-100(Fe) or Fe-BTC have the same zeolite MTN topology, the unit cell parameters are: a, b, c = 73.340 Å and V = 394481 Å3 with a space group of F d 3 m^{30,45}. The mesoporous cages are 2.5 and 2.9 nm in diameter, and can be accessed via microporous windows of 0.55 and 0.85 nm in diameter. The Miller indices, which describe the crystallographic planes and directions, are described in table S1. This unique crystal architecture allows metal ions to diffuse in, while preventing large organic interferent compounds from entering.

Next, Fe-BTC is tested for its BET surface area via nitrogen adsorption measurements (Figure 2B). The as-synthesized Fe-BTC exhibits a typical Type I adsorption isotherm and has a relatively high BET surface area of 2677 m² g-1 (Table 1), which is consistent with other studies in the literature⁴⁵. The high BET surface area (>2000 m² g¹) and high crystallinity indicate a high quality material which is used for the subsequent Fe-BTC/PpPDA synthesis. After Fe-BTC/PpPDA is synthesized, PXRD is carried out to confirm the structural integrity of the crystal structure. Figure 2A shows the diffraction pattern of the Fe-BTC/PpPDA is identical to Fe-BTC, illustrating that the *in-situ* polymerization doesn't impact material crystallinity. Next, nitrogen adsorption measurements are performed on Fe-BTC/PpPDA. The introduction of poly(p-phenylenediamine) (PpPDA) polymer to the system decreases the BET surface area to 1243 m² g-1. The BET surface area drops due to the introduction of the polymer occupying part of the MOF's available pore

space²⁹. However, even with this reduction in surface area, the material retains a high BET surface area and exceptional adsorption properties, particularly for gold.

The Fe-BTC and Fe-BTC/PpPDA are next analyzed via ATR-IR to provide information about the chemical composition and structure of the materials³⁷ (Figure S2). ATR-IR is employed to elucidate and identify functional groups within the materials. The Fe-BTC is analyzed first, and it is found that from 600 - 900 cm⁻¹, there are out-of-plane bending modes of substituted aromatics³⁷. From 1200 - 1400 cm⁻¹, there are C-H bending modes in alkanes and aliphatic substituents. From 1400 - 1600 cm⁻¹, aromatic ring structures have C-H bending modes. From 1600 - 1800 cm⁻¹, there are also C=O stretching modes in carbonyl compounds. These functional groups are all present in the organic ligand that makes up the composition of Fe-BTC. The Fe-BTC/PpPDA maintains the same Fe-BTC functional groups, but the intensity of the peaks is reduced by approximately half.

The Fe-BTC and Fe-BTC/PpPDA are analyzed via TGA to study the thermal stability and composition of the materials (Figure S3) as well. All materials have a sharp 15-20% drop in weight from 0°C - 100°C, due to moisture in the sample. The materials weight percent (wt. %) decreases at a slow steady rate until 275°C, where the curves drop drastically until 320°C. This is due to the decomposition of the organic ligands present leaving only the inorganics left in the sample. It highlights the materials will be thermally stable for the application area we envision. The material's weight remains constant at 20% weight, which is consistent with previous studies^{29,30}.

Fe-BTC/PpPDA is synthesized as submicron sized particles between 250 nm and 500 nm in diameter, which are currently too small to be implemented in any traditional column filter device. Under a continuous flow operation, the highly fine powder is either lost or forms a sludge that increases pressure and decreases flow rate along the column bed. To mitigate this, the materials must be structurally optimized to prevent pressure drops and loss of material during the continuous flow operation (Figure 1C). Therefore, we employ disc granulation as an agglomeration methodology (Figure S1) and 10 wt. % fluorinated binder is introduced to Fe-BTC/PpPDA by physical mixing of the materials via a mortar and pestle. The binder aids in particle size formation and strength³². Disc granulation allows the formation of the fine Fe-BTC/PpPDA particles into larger spherical granules up to 1000 μm in diameter by a gravity tumble mechanism³². After granulation, different size G/Fe-BTC/PpPDA granules are sieved out ranging from <53 μm, 53 - 106 μm, 106 - 125 μm, 250 - 500 μm and 500 - 800 μm (Figure S4). Final freeze drying and

heating steps, as detailed in the Methods, are used to make a mechanically more stable material named Structured Fe-BTC/PpPDA, which demonstrate substantially improved performance in continuous flow experiments, as shown in the next section.

Comprehensive characterization of Structured Fe-BTC/PpPDA, characterization was first performed. The PXRD shows that the MOF's structural integrity is maintained after adding the binder, freeze drying, and heating steps (Figure 2A). After PXRD, the BET surface area for Structured Fe-BTC/PpPDA is assessed via nitrogen adsorption. The BET surface area decreases to 750 m² g⁻¹ (Figure 2B, Table 1), which is most likely due to addition of the binder. The material still has a high BET surface area that is consistent with other high performing porous framework materials such as mesoporous covalent organic frameworks (COFs) or Silicas, where their BET surface area can also reach up to approximately ~700 m² g⁻¹ ^{46,47}. Further, Horvath-Kawazoe pore distribution curves were obtained (Figure S15). It is observed that there is a reduction in peak heights of the Structured Fe-BTC/PpPDA curve, approximately by half, compared to Fe-

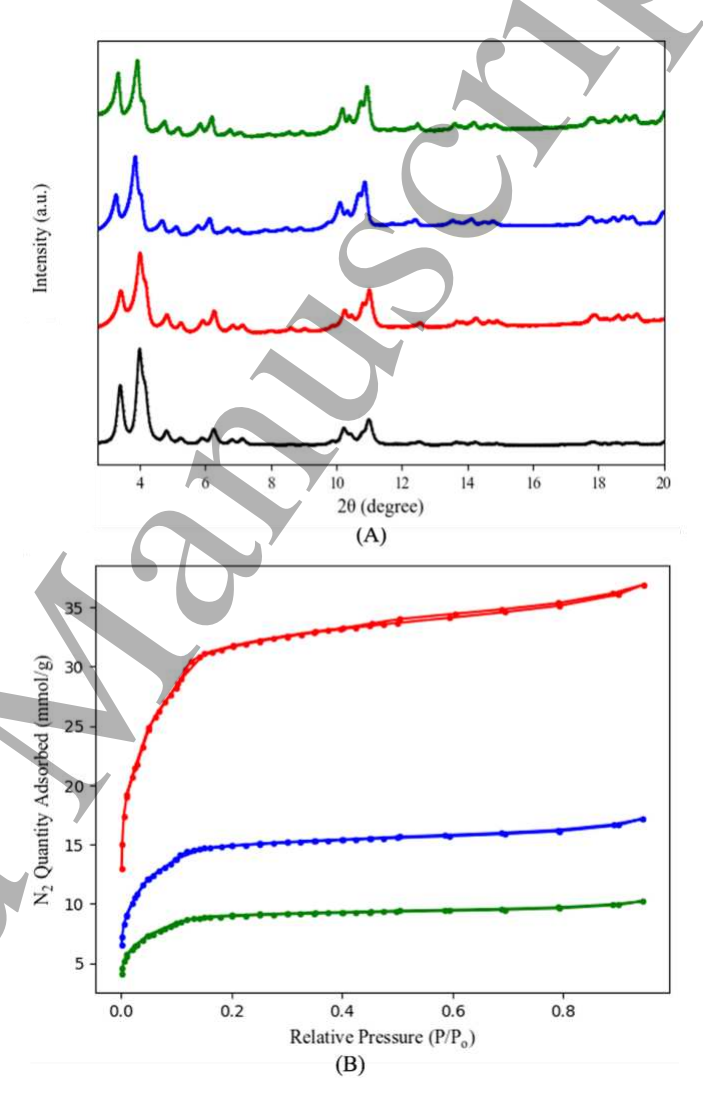


Figure 2. (A) Powder x-ray diffraction and **(B)** nitrogen adsorption isotherms of simulated Fe-BTC (black), Fe-BTC (red) (BET surface area = $2677 \text{ m}^2 \text{ g}^{-1}$), Fe-BTC/PpPDA (blue) (BET surface area = $1243 \text{ m}^2 \text{ g}^{-1}$) and Structured Fe-BTC/PpPDA (green) (BET surface area = $750 \text{ m}^2 \text{ g}^{-1}$). The diffraction patterns retain the same peaks demonstrating structural integrity post *in-situ* polymerization and structuring. There is also a decrease in BET surface area after each step to Structured Fe-BTC/PpPDA.

BTC. We surmise, this decrease is attributed to pore blocking caused by the addition of a binder and polymer in the MOF. Throughout the synthesis and agglomeration processes, the final

Structured Fe-BTC/PpPDA still maintains high crystallinity and a high BET surface area, which are vital for high performance in adsorption separation processes.

Structured Fe-BTC/PpPDA was also analyzed via ATR-IR to identify functional groups within the materials (Figure S2). The Structured Fe-BTC/PpPDA maintains the Fe-BTC/PpPDA composition, with the new addition of peaks at 770 - 800 cm⁻¹, 880 - 900 cm⁻¹, and 1100 - 1285

Material	BET Surface Area (m ² g ⁻¹)	Total Pore Volume (cm³/g)
Fe-BTC	2677	25.31
Fe-BTC/PpPDA	1243	17.91
Structured Fe-BTC/PpPDA	750	13.02

Table 1. BET Surface Area (m² g⁻¹) and Total Pore Volume (cm³/g)

cm⁻¹. A C-F stretching vibration is observed between 770 - 800 cm⁻¹, which is a functional group present within the binder³⁸. From 880 - 900 cm⁻¹, there are out-of-plane bending modes of substituted aromatics as well as a C-O stretching bonds from 1100 - 1285 cm⁻¹ ³⁷. The Structured Fe-BTC/PpPDA is also analyzed via TGA and follows the same trends as Fe-BTC and Fe-BTC/PpPDA (Figure S4).

Structured Fe-BTC/PpPDA is then analyzed via SEM and EDS (Figure 3) to provide high-resolution images of the surface topography, morphology, and provide an elemental analysis of the material. Figure 3A shows SEM images of 250 µm Structured Fe-BTC/PpPDA granules used in our column and batch experiments. A close-up image of the Structured Fe-BTC/PpPDA particle shows smaller particles or subunits, indicating crystallites between 200 nm and 500 nm are present and aggregated. EDS imaging demonstrates the presence of iron, nitrogen, and fluorine which is uniformly distributed through the Structured Fe-BTC/PpPDA material (Figure 3B).

Figures S5A-8A illustrate the XPS survey spectrum of Structured Fe-BTC/PpPDA. The O 1s spectrum of the Structured Fe-BTC/PpPDA (Figure S5A) shows the presence of O-C at 531.3 eV and Fe-O at 529.2 eV. The four components that were identified in the C 1s spectra (Figure S6A) were at ~284.6 eV, ~286.1 eV, ~288.4 eV, ~290.8 eV corresponding to CHx C-NH₂, C-O/C-N, O-C=O, and π - π *, respectively³⁹. As seen in Figure S7A, the peaks at ~713.4 eV and ~729.4 eV correspond to Fe³⁺ while the peaks at ~711.0 eV and 724.8 eV correspond to Fe²⁺. The large

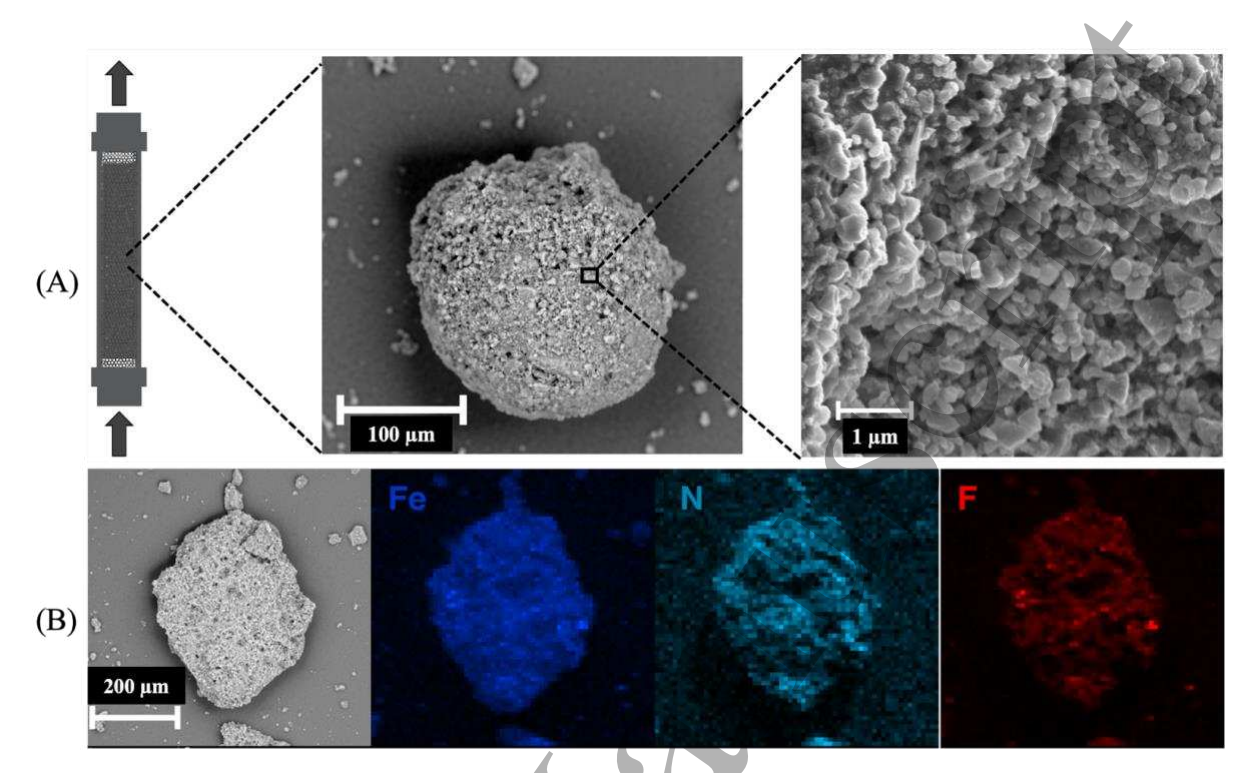


Figure 3. (A) SEM images of a 250 μm Structured Fe-BTC/PpPDA in 100 μm and 1 μm scale. A close-up image of the Structured Fe-BTC/PpPDA particle reveals subunits within the particle with sizes between 200 nm and 500 nm. **(B)** SEM and EDS of Structured Fe-BTC/PpPDA on a 200 μm scale indicating the iron (Fe) (dark blue) MOF, nitrogen (N) (light blue) throughout the material, and the fluorinated (F) (red) binder throughout the material.

satellite peak at \sim 716.8 eV indicates the presence of both Fe²⁺ and Fe³⁺. The two main peaks identified in the N 1s spectra (Figure S8) were R₂NH and =NR at \sim 400.1 eV and \sim 399.0 eV, respectively indicating successful *in-situ* polymerization of poly-p-phenylenediamine.

Structured Fe-BTC/PpPDA Batch Extraction Experiments

Batch Au³⁺ adsorption experiments were conducted to observe that Structured Fe-BTC/PpPDA maintains its selectivity for gold (Figure 4). As previously reported just for the composite²⁹, Fe-BTC/PpPDA does not extract hard ions such as Ca²⁺, Mg²⁺, Na⁺ and K⁺, but readily extracts and concentrates Au ions from a fresh surface water source. The Structured Fe-BTC/PpPDA material maintains the same metal extraction properties as it does not extract the hard ions and concentrates Au ions from fresh water sources (Figure 4). The batch extraction kinetics experiments illustrate that as particles increase in size, the rate of extraction decreases (Figure S9), suggesting that engineering smaller but stable particle sizes is necessary to maximize transport and diffusion of gold ions in the adsorbent particles. Compared to the pristine composite, the binder may also block active sites where otherwise the adsorption-reduction processes for gold capture would occur. The

rate of gold extraction also decreases as the water system is changed from tap water to creek water (Figure S9). The creek water contains a larger number of ionic species that may slow down gold capture. Although Structured Fe-BTC/PpPDA system remains highly selective for gold in the complex creek water, the high concentration of Mg²⁺ (~40 ppm), Ca^{2+} (~80 ppm), SO_3^{2-} (~20 ppm) and Na⁺ (~40 ppm) may impact the surface charge of the material and thus impact the electrostatic interaction of Au³⁺ and the functional sites within the adsorbent. In general, smaller-

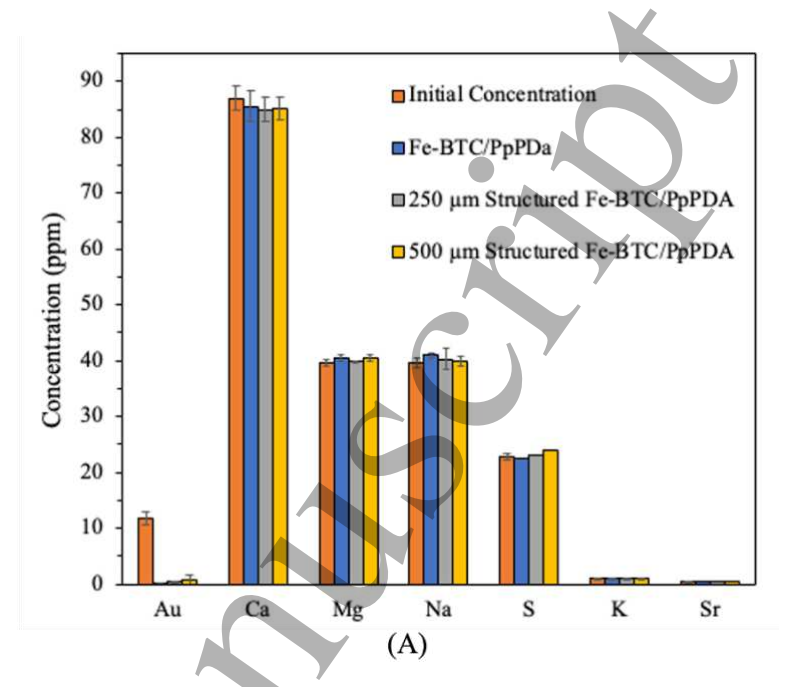


Figure 4. Evaluation of gold extraction from Strawberry Creek water using powder Fe-BTC/PpPDA (light blue), 250 um Structured Fe-BTC/PpPDA granules (gray), and 500 um Structured Fe-BTC/PpPDA granules (yellow). Concentration of metals before and after overnight mixing of powder/particles in the gold spiked (10 ppm) Strawberry Creek water.

sized MOFs tend to have a higher surface area to volume ratio, which makes them more effective at capturing and absorbing particles, specifically Au in our case.

The polymer (PpPDA) pinned along the inner pore surface of the MOF (Fe-BTC) is the fundamental contributor to the enhanced gold extraction capability of the MOF/Polymer system²⁹. The Au³⁺ ions diffuse into the porous network and interact with the amine functional groups that are along the backbone of the polymer. This results in an electron transfer event that occurs between the amine functional groups and Au³⁺ ions. The amine functional groups are oxidized, while the Au³⁺ ions are reduced to neutral state Au⁰ precipitating out within the highly porous framework. The combined use of PXRD and XPS as shown in Figure 6 confirms this efficient reduction of Au³⁺ to its metallic state Au⁰. The synergistic combination of the electron rich poly(para-phenylenediamine) with the highly porous Fe-BTC results in a redox-active MOF/Polymer composite with exceptional gold scavenging capabilities.

Structured Fe-BTC/PpPDA Performance in Small Packed Bed Columns

In the first experiment, 500 µm G/Fe-BTC/PpPDA was loaded into a small column, labeled Column 1 (Figure 5). 500 µm granulated G/Fe-BTC/PpPDA particles would initially maintain a consistent pressure and flow rate, but after 2.5 hours an increase in pressure is observed (Figure 5B). At 5 hours, the pressure is measured at 5 psi, but then increases 4-fold to 20 psi after 20 hours of continuous flow operation (Figure 5B). The gradual increase in pressure over time indicates that the G/Fe-BTC/PpPDA are fracturing during the continuous flow operation and form sludge-like consistency across the column bed, thereby compromising flow rate. Column 1 reaches 45% of breakthrough concentration at hour 11. Interestingly, at hour 25 we observe over 99% of the gold is being captured by the column. This can be explained by the significant pressure increase after hour 10, which significantly lowered the flow rate resulting in a longer retention time in the column. This increase in retention time allows for higher gold adsorption and diffusion into the column particles. Therefore, it was important to mitigate particle fracturing and pressure increase issues in our continuous flow packed bed column experiments.

Structured Fe-BTC/PpPDA, which adds freeze drying and heating steps, is used to prevent the aforementioned problems. 250 µm and 500 µm size particles of Structured Fe-BTC/PpPDA were employed for the remainder of the study, since particles less than 250 µm would create a sludge-like consistency compromising the column experiments. A 10 ppm Au aqueous solution is pumped through the columns at a flow rate of 10 mL per minute for 34 hours. The influent, which is the water before it has passed through the column, is sampled to determine consistent initial Au concentration. The effluent, which is the water once it has passed through the column, is sampled hourly. These samples are then analyzed via ICP-OES to determine the gold concentration and create breakthrough curves (Figure 5A).

500 µm Structured Fe-BTC/PpPDA shows a slight decrease in performance but a stable continuous flow experiment over 30 hours with only a slight increase in pressure over the duration of the experiment. (Figure 5A,5B). From hour 1 to 7, it was observed that there is a steady increase in Au saturation reaching 60%. At hour 22, the Column 2 and Column 3 reach near saturation, with 80% breakthrough (Figure 5A). Experiments employing 250 µm Structured Fe-BTC/PpPDA granules illustrate an increase in performance and follow similar trends (Figure 3A, Column 4 (olive), Column 5 (aquamarine), and Column 6 (salmon)). For the first 3 hours, over 90% of gold is captured within the column. After hour 3, there is a steady increase in gold concentration in the effluent reaching 40% in breakthrough 9 hours. At hour 23, it is observed that the column is

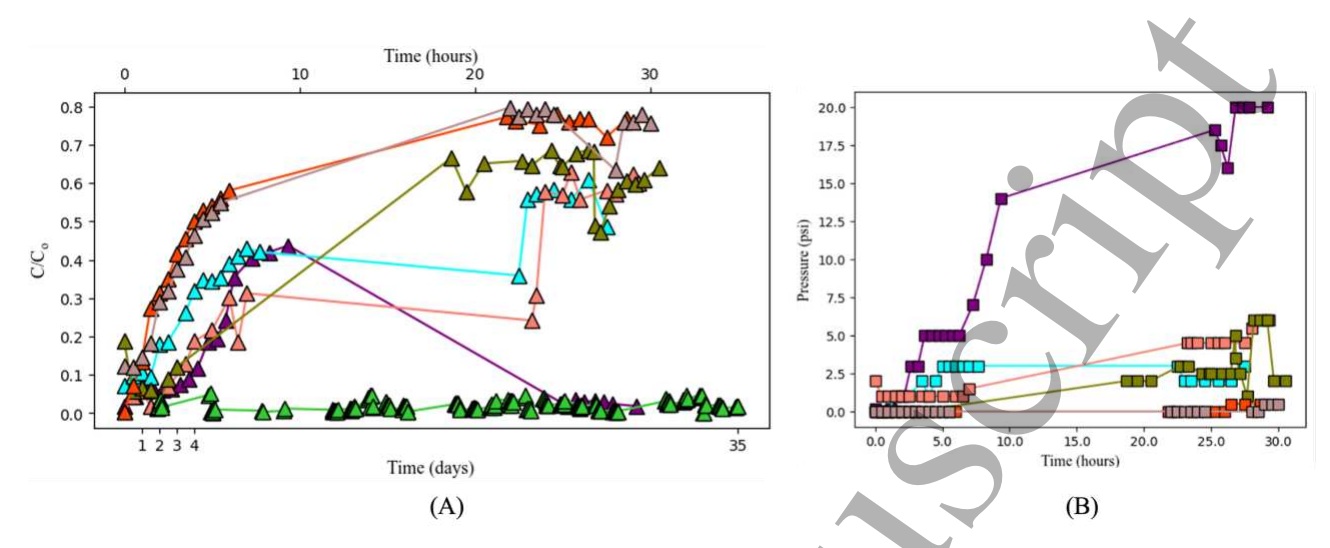


Figure 5. (A) Breakthrough curves for Columns 1-7 with C/C_o (effluent concentration over initial concentration) vs. Time (hours) and C/C_o vs. Time (days) for column 7 **(B)** Pressures for Columns 1-6 with Pressure (psi) vs. Time (hours). Column 1 = 500 μm G/Fe-BTC/PpPDA (purple), Column 2 = 500 μm Structured Fe-BTC/PpPDA (orange/red), Column 3 = 500 μm Structured Fe-BTC/PpPDA (rosy brown), Column 4 = 250 μm Structured Fe-BTC/PpPDA (olive), Column 5 = 250 μm Structured Fe-BTC/PpPDA (aquamarine), Column 6 = 250 μm Structured Fe-BTC/PpPDA (salmon), and Column 7 = 250 μm Structured Fe-BTC/PpPDA (line green).

capturing approximately 55% of the gold until the end of the experiment at hour 31. This suggests that smaller granule size will increase performance of the column. Next, the Structured Fe-BTC/PpPDA Post Filter material is characterized.

Structured Fe-BTC/PpPDA Post Filter Characterization

The PXRD patterns are identical for all Structured Fe-BTC/PpPDA Post Filter materials, shown in Figure 5 with Column 4's diffraction pattern shown in Figure 6A, demonstrating. the structure of the MOF maintains its crystal structure post filter operation (Figure 6A). Furthermore, PXRD confirmed the presence of neutral state Au with diffraction peaks appearing at 38.2°, 44.4°, 64.5°, and 77.6° ⁴². Next, the BET surface area was found to be 621 m² g⁻¹, about 17% less than the assynthesized Structured Fe-BTC/PpPDA (Figure S10). The ATR-IR data for the Structured Fe-BTC/PpPDA Post Filter was not noticeably different from the as-synthesized Structured Fe-BTC/PpPDA. The TGA data (Figure S3) of Column 4 Structured Fe-BTC/PpPDA Post Filter also show similar thermal stability as the as-synthesized Structured Fe-BTC/PpPDA before column experiments. Samples were then digested in aqua regia, and ICP-OES was employed to determine the gold weight % in the samples. It was determined that the gold wt.% ranged from 9 - 16 wt. % between all the *small* column experiments (Figure S11).

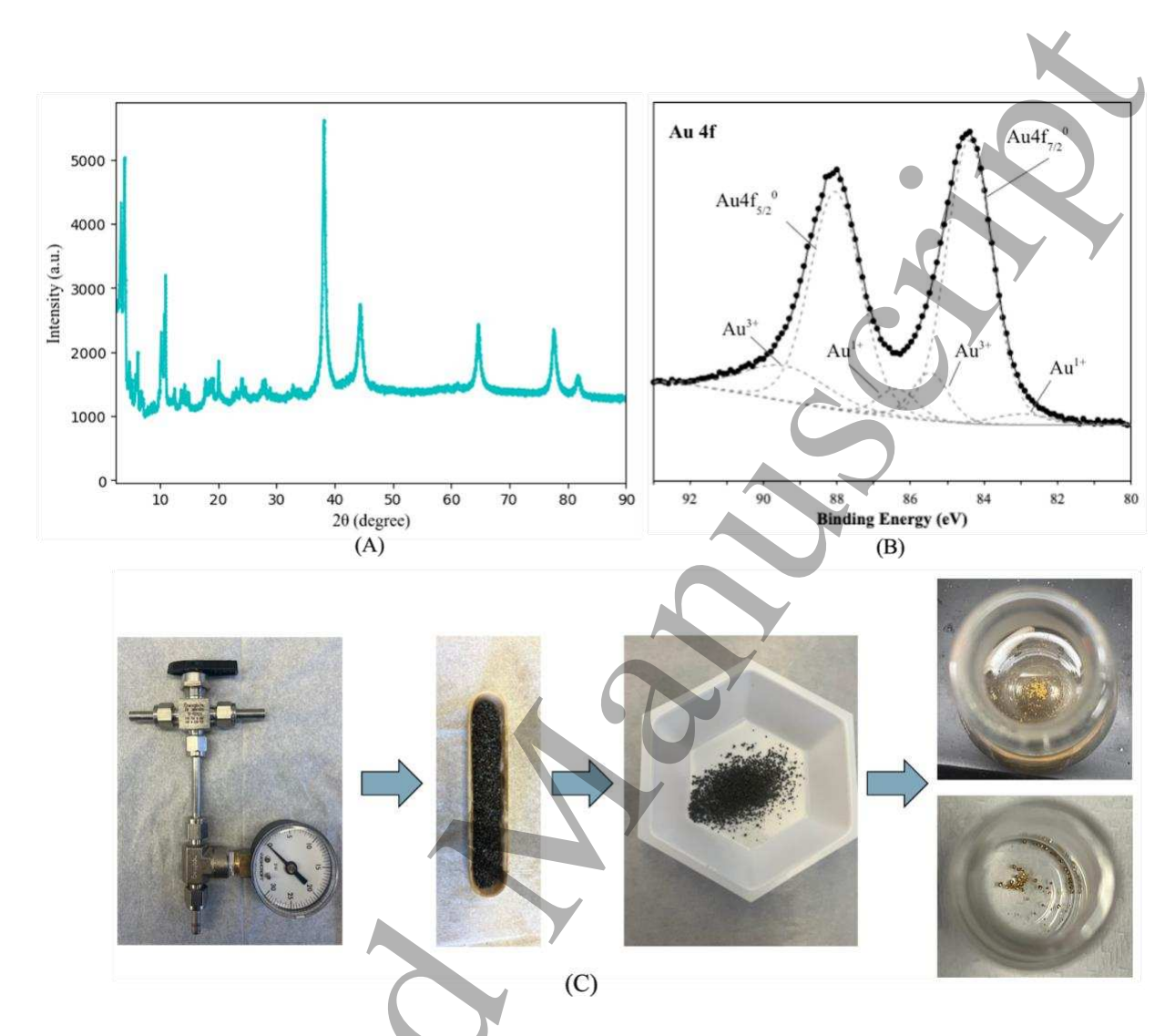


Figure 6. Structured Fe-BTC/PpPDA Post-Filter on **(A)** powder x-ray diffraction and **(B)** X-ray photoelectron spectrum (XPS) curve. **(A)** The structure of the MOF maintains its crystal structure post filter operation. **(B)** Further, PXRD confirmed the presence of neutral state Au with diffraction peaks appearing at 38.2°, 44.4°, 64.5°, and 77.6°. XPS confirmed the reduction of Au³⁺ to Au⁰ during the column operation. **(C)** To separate the gold once it has been adsorbed to the material, the Structured Fe-BTC/PpPDA Post Filter was placed in a 1300 Thermolyne Furnace at 400°C for 5 hours and then soaked in concentrated hydrochloric acid.

XPS confirmed the reduction of Au³⁺ to Au⁰ during the column operation (Figure 6B). Curve fitting of the Au 4f spectra also showed the presence of 1+ and 3+ states on the surface of the post-column material, which also indicates the incomplete reduction of Au³⁺. Furthermore, SEM coupled with EDS was employed to determine the morphology of the Post-Filter Structured Fe-BTC/PpPDA materials (Figure S12). Interestingly, it is observed that there are gold particles present on the outside of the materials after the continuous flow operation. Surface redox processes may be a dominant mechanism over mass transport through the pores of the Structured Fe-

BTC/PpPDA or it may be a mixture of both. It seems there are specific nucleation sites where gold particles can grow during the continuous flow operation.

The O 1s XPS spectra for Column 4 Structured Fe-BTC/PpPDA Post Filter shows O-C at 531.3 eV and O=C at 533.7 eV, but with a lower peak of Fe-O compared to Structured Fe-BTC/PpPDA⁴³. The same peaks were identified in Figure S6B with Column 4 Structured Fe-BTC/PpPDA Post Filter, except with a much lower intensity of the π - π * peak. The Fe 2p spectra (Figure S7) for both Structured Fe-BTC/PpPDA and Column 4 Structured Fe-BTC/PpPDA Post Filter are similar. As seen in Figure S5-8, the peaks at \sim 713.4 eV and \sim 729.4 eV correspond to Fe³⁺ while the peaks at ~711.0 eV and 724.8 eV correspond to Fe²⁺. The large satellite peak at ~716.8 eV indicates the presence of both Fe²⁺ and Fe³⁺, which does not appear to change in the post-filter state. Further, the peak fitting of N shows that there is a shift to a lower binding energy when comparing Structured Fe-BTC/PpPDA to Post-Filter Structured Fe-BTC/PpPDA (Figure S8). The R2NH functional groups are oxidized to =NR and the Au³⁺ ions are reduced to Au⁰. This indicated that an electron transfer event is happening between the nitrogen functional groups along the polymer backbone and the gold ions in solution⁴⁴.

Structured Fe-BTC/PpPDA Performance in Large Packed Bed Column

The data from column 1 (Figure 5A) illustrates that an increase in residence time of the column can increase the gold extraction performance of the Structured Fe-BTC/PpPDA. The aforementioned experiments with the small column experiments have a residence time $(\tau_{PBR})^{44}$ of just 1.52 seconds, which was calculated using equations 1 and 2 below. The bed voidage (Eb) is 0.35 45, L is the length of the column, u₀ is the superficial velocity at the inlet of the column, Q is the flow rate in mL/min, and A is the area of the column.

$$\tau_{PBR} = \frac{\epsilon_b L}{u_o}$$
 (Equation 1)
$$u_o = \frac{Q}{A} = \frac{Q}{\pi r^2}$$
 (Equation 2)

$$u_o = \frac{Q}{A} = \frac{Q}{\pi r^2}$$
 (Equation 2)

The large column experiment was designed with a larger volume (and more material) to increase the residence time by 50x to 77 seconds, or 1.3 minutes, to determine how much greater extraction efficiency can be achieved. The new *large* column (Column 7) was scaled up to have an internal diameter of 0.375 inches and a height of 9.85 inches. After calibration, the column is filled with 6.0 g of 250 µm Structured Fe-BTC/PpPDA, 2.0 g of glass beads (1.0 g on both ends of the

column), and glass wool with a diameter of 0.375 inches at the tip of the column. The newly filled column is pumped with distilled water for 5 minutes to ensure a consistent 5 mL min⁻¹ flow rate. After 35 days of consistent continuous pumping of a 10 ppm Au tap water solution, there is still no breakthrough of gold in the effluent (Figure 5A). As a result, the Au wt. % within the Structured Fe-BTC/PpPDA is calculated to be approximately 42 wt.% based on the large column's breakthrough curve data (Figure S14).

4. Conclusion

Structured Fe-BTC/PpPDA is a novel redox active MOF/polymer composite that provides the precision separation of gold from complex water mixtures under a continuous flow operation. Here, we demonstrate a method to control the particle size, so that different MOF and MOF composite materials can be easily implemented into continuous processes and assessed for continuous industrial process viability. The Structured Fe-BTC/PpPDA 250 µm and 500 µm particles maintain their crystalline framework structure, remain highly porous, and selectively extract gold from complex water mixtures. Further, under a continuous operation we demonstrate that these materials can maintain a low pressure differential and consistent flow rate for over 35 days concentrating 42 wt. % gold thus far in the column. We envision that judicial selection of MOF and polymer building blocks and post-synthetic modification of the polymer backbone will lead to new materials that are selective towards other critical metals of interest to the public. When the MOF/Polymer material is incorporated into a filter device, it has the potential to impact and revolutionize how we mine or recover critical metals of environmental, economic and energy interest.

Ethical Statement

D.T.S. and D.H. have a financial interest in Sunchem Inc., a start-up company working on commercializing novel materials and technologies for the precision separation of critical metals.

Acknowledgements

Work at the Molecular Foundry was supported by the Office of Science, Office of Basic Energy Sciences, of the U.S. Department of Energy under Contract No. DE-AC02-05CH11231. Work was also supported by the National Science Foundation under NSF award number 2151734 and the Cyclotron Road program, especially Melanie Sonsteng, Todd Pray and Thomas Kirchstetter,

supported by the U.S. Department of Energy's Advanced Materials and Manufacturing Technologies Office. The authors would like to graciously thank Yi Liu, Eric Dailing, Steve Shelton, Tracy Mattox, Tevye Kuykendall, Anne Pham, David Britt and Mel Leutkens for their ongoing support and helpful discussions. The authors would also like to thank Activate for their ongoing support, resources, and mentorship especially Jill Fuss and Katie Sharp.

Data Availability Statement

All data that support the findings of this study are included within the article (and any supplementary files).

References

- [1] Hendon CH, Rieth AJ, Korzynski MD, Dinca M. Grand Challenges and Future Opportunities for Metal-Organic Frameworks. *ACS Central Sci.* 2017 Jun;3(6):554–63.
- [2] Kiprono NR, Smolinski T, Rogowski M, Chmielewski AG. The State of Critical and Strategic Metals Recovery and the Role of Nuclear Techniques in the Separation Technologies Development: Review. *Separations*. 2023 Feb;10(2):112.
- [3] M. Izatt R, R. Izatt S, L. Bruening R, E. Izatt N, A. Moyer B. Challenges to achievement of metal sustainability in our high-tech society. *Chemical Society Reviews*. 2014;43(8):2451–75.
- [4] Moss R, Tzimas E, Kara H, Willis P, Kooroshy J. Critical Metals in Strategic Energy Technologies Assessing Rare Metals as Supply-Chain Bottlenecks in Low-Carbon Energy Technologies. Publications Office of the European Union. 2011.
- [5] Gold Price Chart, Live Spot Gold Rates, Gold Price Per Ounce/Gram. BullionVault. 2023. https://www.bullionvault.com/gold-price-chart.do
- [6] Howarth AJ, Liu Y, Li P, Li Z, Wang TC, Hupp J, et al. Chemical, thermal and mechanical stabilities of metal-organic frameworks. *Nat Rev Mater.* 2016 Mar;1(3):15018.
- [7] Hunt ST, Milina M, Alba-Rubio AC, Hendon CH, Dumesic JA, Roman-Leshkov Y. Self-assembly of noble metal monolayers on transition metal carbide nanoparticle catalysts. *Science*. 2016 May 20;352(6288):974–8.
- [8] Lee J, Farha OK, Roberts J, Scheidt KA, Nguyen ST, Hupp JT. Metal-organic framework materials as catalysts. *Chem Soc Rev.* 2009;38(5):1450–9.
- [9] Althues H, Henle J, Kaskel S. Functional inorganic nanofillers for transparent polymers. *Chemical Society Reviews*. 2007;36(9):1454–65.
- [10] Kerrich R. Nature's Gold Factory. Science. 1999 Jun 25;284(5423):2101–2.
- [11] McHugh JB. Concentration of gold in natural waters. *Journal of Geochemical Exploration*. 1988 Jan 1;30(1):85–94.
- [12] Setyawati MI, Xie J, Leong DT. Phage Based Green Chemistry for Gold Ion Reduction and Gold Retrieval. *ACS Appl Mater Interfaces*. 2014 Jan 22;6(2):910–7.
- [13] Farha OK, Yazaydin AO, Eryazici I, Malliakas CD, Hauser BG, Kanatzidis MG, et al. De novo synthesis of a metal-organic framework material featuring ultrahigh surface area and gas storage capacities. *Nat Chem.* 2010 Nov;2(11):944–8.
- [14] Furukawa H, Cordova KE, O'Keeffe M, Yaghi OM. The Chemistry and Applications of Metal-Organic Frameworks. *Science*. 2013 Aug 30;341(6149):1230444.
- [15] Guillerm V, Kim D, Eubank JF, Luebke R, Liu X, Adil K, et al. A supermolecular building approach for the design and construction of metal-organic frameworks. *Chem Soc Rev.* 2014 Aug 21;43(16):6141–72.

- [16] Farha OK, Eryazici I, Jeong NC, Hauser BG, Wilmer CE, Sarjeant AA, et al. Metal–Organic Framework Materials with Ultrahigh Surface Areas: Is the Sky the Limit? *J Am Chem Soc.* 2012 Sep 12;134(36):15016–21.
- [17] Furukawa H, Ko N, Go YB, Aratani N, Choi SB, Choi E, et al. Ultrahigh Porosity in Metal-Organic Frameworks. *Science*. 2010 Jul 23;329(5990):424–8.
- [18] Long JR, Yaghi OM. The pervasive chemistry of metal—organic frameworks. *Chem Soc Rev.* 2009 Apr 21;38(5):1213–4.
- [19] Lu G, Li S, Guo Z, Farha OK, Hauser BG, Qi X, et al. Imparting functionality to a metal-organic framework material by controlled nanoparticle encapsulation. *Nat Chem.* 2012 Apr;4(4):310–6.
- [20] Wang S, McGuirk CM, d'Aquino A, Mason JA, Mirkin CA. Metal-Organic Framework Nanoparticles. *Adv Mater*. 2018 Sep 13;30(37):1800202.
- [21] Adil K, Belmabkhout Y, Pillai RS, Cadiau A, Bhatt PM, Assen AH, et al. Gas/vapour separation using ultra-microporous metal-organic frameworks: insights into the structure/separation relationship. *Chem Soc Rev.* 2017 Jun 7;46(11):3402–30.
- [22] Stock N, Biswas S. Synthesis of Metal-Organic Frameworks (MOFs): Routes to Various MOF Topologies, Morphologies, and Composites. *Chem Rev.* 2012 Feb 8;112(2):933–69.
- [23] Batten SR, Champness NR, Chen XM, Garcia-Martinez J, Kitagawa S, Ohrstrom L, et al. Terminology of metal-organic frameworks and coordination polymers (IUPAC Recommendations 2013). *Pure Appl Chem.* 2013;85(8):1715–24.
- [24] Bloch ED, Murray LJ, Queen WL, Chavan S, Maximoff SN, Bigi JP, et al. Selective Binding of O-2 over N-2 in a Redox-Active Metal-Organic Framework with Open Iron(II) Coordination Sites. *J Am Chem Soc.* 2011 Sep 21;133(37):14814–22.
- [25] Bloch ED, Queen WL, Krishna R, Zadrozny JM, Brown CM, Long JR. Hydrocarbon Separations in a Metal-Organic Framework with Open Iron(II) Coordination Sites. *Science*. 2012 Mar 30;335(6076):1606–10.
- [26] Li J, Wang X, Zhao G, Chen C, Chai Z, Alsaedi A, et al. Metal—organic framework-based materials: superior adsorbents for the capture of toxic and radioactive metal ions. *Chemical Society Reviews*. 2018;47(7):2322–56.
- [27] Peng Y, Huang H, Zhang Y, Kang C, Chen S, Song L, et al. A versatile MOF-based trap for heavy metal ion capture and dispersion. *Nat Commun.* 2018 Jan 15;9(1):187.
- [28] Sun DT. Construction of MOF/Polymer Composites for Metal Ion Capture. [Lausanne]: EPFL; 2020.
- [29] Sun DT, Gasilova N, Yang S, Oveisi E, Queen WL. Rapid, Selective Extraction of Trace Amounts of Gold from Complex Water Mixtures with a Metal–Organic Framework (MOF)/Polymer Composite. *J Am Chem Soc.* 2018 Dec 5;140(48):16697–703.
- [30] Sun DT, Peng L, Reeder WS, Moosavi SM, Tiana D, Britt DK, et al. Rapid, Selective Heavy Metal Removal from Water by a Metal–Organic Framework/Polydopamine Composite. *ACS Cent Sci.* 2018 Mar 28;4(3):349–56.
- [31] Xu GR, An ZH, Xu K, Liu Q, Das R, Zhao HL. Metal organic framework (MOF)-based micro/nanoscaled materials for heavy metal ions removal: The cutting-edge study on designs, synthesis, and applications. *Coordination Chemistry Reviews*. 2021 Jan 15;427:213554.
- [32] Wang Z, Liu L, Li Z, Goyal N, Du T, He J, et al. Shaping of Metal-Organic Frameworks: A Review. *Energy Fuels*. 2022 Mar 17;36(6):2927–44.
- [33] Ali I, Gupta VK. Advances in water treatment by adsorption technology. *Nat Protoc.* 2006 Dec;1(6):2661–7.
- [34] Furukawa H, Gándara F, Zhang YB, Jiang J, Queen WL, Hudson MR, et al. Water Adsorption in Porous Metal–Organic Frameworks and Related Materials. *J Am Chem Soc.* 2014 Mar 19;136(11):4369–81.
- [35] Abdolali A, Ngo HH, Guo W, Zhou JL, Zhang J, Liang S, et al. Application of a breakthrough biosorbent for removing heavy metals from synthetic and real wastewaters in a lab-scale continuous fixed-bed column. *Bioresource Technology*. 2017 Apr 1;229:78–87.

- [36] Macrae CF, Edgington PR, McCabe P, Pidcock E, Shields GP, Taylor R, et al. Mercury: visualization and analysis of crystal structures. Journal of Applied Crystallography. 2006;39(3):453.
- [37] Silverstein RM, Webster FX, Kiemle DJ, Bryce DL. Spectrometric identification of organic compounds. 8th ed. Hoboken, NJ: Wiley; 2015.
- [38] Nakamoto K. *Infrared and Raman Spectra of Inorganic and Coordination Compounds*. Hoboken, NJ, USA: John Wiley & Sons, Inc.; 2008.
- [39] Song Y, Duan F, Zhang S, Tian JY, Zhang Z, Wang ZW, Liu CS, Xu WM, Du M. Iron oxide@ mesoporous carbon architectures derived from an Fe (II)-based metal organic framework for highly sensitive oxytetracycline determination. *Journal of Materials Chemistry A.* 2017;5(36):19378-89.
- [40] Benjamin MM, Lawler DF. Water quality engineering: physical/chemical treatment processes. Hoboken, N.J. John Wiley & Sons; 2013. 878 p.
- [41] Schoedel A, Ji Z, Yaghi OM. The role of metal—organic frameworks in a carbon-neutral energy cycle. Nat Energy. 2016 Apr 4;1(4):1–13.
- [42] Xia Y, Xia X, Peng HC. Shape-Controlled Synthesis of Colloidal Metal Nanocrystals: Thermodynamic versus Kinetic Products. *J Am Chem Soc.* 2015 Jul 1;137(25):7947–66.
- [43] Liang R, Jing F, Shen L, Qin N, Wu L. MIL-53 (Fe) as a highly efficient bifunctional photocatalyst for the simultaneous reduction of Cr (VI) and oxidation of dyes. *Journal of hazardous materials*. 2015 Apr 28;287:364-72.
- [44] Moulder JF, Stickle WF, Sobol PE, Bomben KD. *Handbook of X Ray Photoelectron Spectroscopy:* A Reference Book of Standard Spectra for Identification and Interpretation of Xps Data. Eden Prairie, Minn.: Physical Electronics; 1979.
- [45] P. Horcajada, S. Surblé, C. Serre, D-Y Hong, Y-K Seo, J-S Chang, J-M Grenèche, I. Margiolaki, and G. Férey. Synthesis and catalytic properties of MIL-100(Fe), an iron(III) carboxylate with large pores, Chem. Commun., 2007, 2820 2822.
- [46] D. Chandra, T. Yokoi, T. Tatsumi and A. Bhaumik. Highly Luminescent Organic-Inorganic Hybrid Mesoporous Silicas Containing Tunable Chemosensor inside the Pore Wall, Chem. Mater. 2007, 19, 22, 5347-5354.
- [47] S. K. Das, S. Mishra, K. Manna, U. Kayal, S. Mahapatra, K. D. Saha, S. Dalapati, G. P. Das, A. A. Mostafa, A. Bhaumik. A new triazine based π -conjugated mesoporous 2D covalent organic framework: its in vitro anticancer activities, Chem. Commun., 2018, 54, 11475 11478.
- [48] K. N. Han, S. Bernardi, L. Wang and D. J. Searles. Water diffusion in zeolite membranes: Molecular dynamics studies on effects of water loading and thermostat, Journal of Membrane Science, 2015, 495, 322 333.

